10.1109/JPHOTOV.2024.3463974 (accepted version)

Design for Increased Defect Tolerance in Metamorphic GaAsP-on-Si Top Cells

Tal Kasher, *Member, IEEE*, Lauren M. Kaliszewski, Daniel L. Lepkowski, *Member, IEEE*, Jacob T. Boyer, *Member, IEEE*, Marzieh Baan, Tyler J. Grassman, *Senior Member, IEEE*, Steven A. Ringel, *Fellow, IEEE*

***Abstract*— To date, the greatest performance limiter in monolithic III-V/Si tandem (multijunction) solar cells, like $GaAs_{0.75}P_{0.25}$/Si, is excess threading dislocation densities (TDD) resulting from the lattice-mismatched heteroepitaxy. Recent developments in low-TDD $GaAs_yP_{1-y}$/Si metamorphic buffers were used to grow standalone $GaAs_{0.75}P_{0.25}$ top cells on Si with a TDD of 4×10^6 cm^{-2}, ~2.5× lower than previous iterations, greatly improving the potential for the production of high-efficiency tandems based on this platform. Nonetheless, these reduced-TDD cells were still found to possess considerable voltage-dependent carrier collection (VDC) losses. As such, to improve J_{SC} and fill factor, without sacrificial reduction in V_{OC}, a doping gradient within the cell base layer was designed and implemented. The updated design reduces VDC losses to levels that would otherwise require further TDD reduction by at least another 2.5× (to ≤ 1.5×10^6 cm^{-2}) in a typical flat doping profile design. Replacing the p$^+$-$Ga_{0.64}In_{0.36}P$ back surface field (BSF) with p$^+$-$Al_{0.2}Ga_{0.8}As_{0.74}P_{0.26}$ provided an additional improvement in both V_{OC} and J_{SC}, yielding device performance equivalent to a 4× TDD reduction in the previous design. The culmination of these design changes results in a new sub cell that outperforms our previous best top cell by ~4.3% absolute AM1.5G efficiency, with increases in fill factor, J_{SC}, and W_{OC} of about 3.3% absolute, 1.9 mA/cm^2, and 0.12 V, respectively. This new design, coupled with the reduced TDD platform, paves a promising path toward development of higher efficiency $GaAs_{0.75}P_{0.25}$/Si tandems upon full device integration.**

***Index Terms*—III-V/Si tandem solar cell, dislocations, semiconductor epitaxial layers, III–V semiconductor material**

I. INTRODUCTION

THE use of Si-based tandem solar cells is a promising avenue for the achievement of high photovoltaic conversion efficiency, surpassing that of single-junction solar cells, but at a nominally lower cost than traditional III-V multijunction cells grown on Ge or III-V substrates. Demonstrated performance of Si-based tandems using top junctions consisting of either III-V compound semiconductors or metal-halide perovskites have now greatly exceeded that of single-junction Si cells [1]. While the impressive results from the halide perovskite-based Si tandems are a subject of intense current interest, the well-known long-term stability and reliability of III-V materials [2], [3] make them an attractive candidate for continued research efforts and are thus the focus of this work.

Approaches for integration of III-V and Si solar cells can be split into three main classifications: mechanical stacking, wafer bonding, and monolithic heteroepitaxial integration. Mechanically stacked triple-junction (3J) GaInP/GaAs//Si cells with as high as 35.9% AM1.5G efficiency have thus far been demonstrated, with champion two-junction (2J) GaAs//Si cells yielding 32.8% [4]. Wafer bonded 3J GaInP/AlGaAs//Si cells with 35.9% efficiency have also been achieved [5]. These results showcase the ultimate potential of the III-V/Si integrated materials system, but both stacking and bonding approaches necessitate complex and heretofore costly fabrication processes that do not readily scale with Si area.

However, heteroepitaxially-integrated III-V/Si solar cells, which do naturally scale with Si substrate area and only require a single starting wafer, pose a different, fundamental challenge due to the need to manage the lattice mismatch within an all-epitaxial monolithic structure. If not adequately mitigated, this mismatch gives rise to a high concentration of performance-degrading threading dislocations within the upper III-V cells. The usual mitigation strategy is to gradually accommodate the mismatch with a compositionally-graded (metamorphic) buffer between the Si and III-V cells. This intentionally-relaxed structure helps to control dislocation dynamics, preventing rampant defect generation that would otherwise occur for a single, highly-mismatched epilayer, thereby lowering the threading dislocation density (TDD) within the III-V device

This work was supported in part by the Department of Energy, Office of Energy Efficiency and Renewable Energy (EERE), under grant DE-EE0007539 and by the National Science Foundation under Grant No. (2047308). The work of D. L. Lepkowski and J. T. Boyer was supported by the NSF-GRFP (DGE-1650114) and NASA-NSTRF (NNX16AM50H) graduate fellowship programs, respectively. *(Corresponding author: Steven A. Ringel).*

Tal Kasher is with the Department of Electrical and Computer Engineering, The Ohio State University, Columbus, OH, 43210, USA (e-mail: kasher.4@osu.edu).

Daniel L. Lepkowski was with The Ohio State University, Columbus, OH, 43210, USA. He is now with New Silicon Corp, 139951, Singapore (e-mail: daniel@nscinnovation.com).

Lauren M. Kaliszewski is with the Department of Material Science Engineering, The Ohio State University, Columbus, OH, 43210, USA. (e-mail: kaliszewski.8@osu.edu).

Jacob T. Boyer was with The Ohio State University, Columbus, OH, 43210, USA. He is now with the HRL Laboratories, Malibu, CA 90265 USA (e-mail: jboyer@hrl.com).

Marzieh Baan is with the Department of Material Science Engineering, The Ohio State University, Columbus, OH, 43210, USA (e-mail: baan.2@osu.edu).

Tyler J. Grassman is with the Department of Electrical and Computer Engineering and the Department of Material Science Engineering, The Ohio State University, Columbus, OH, 43210, USA. (e-mail: grassman.5@osu.edu)

Steven A. Ringel is with the Department of Electrical and Computer Engineering and the Institute for Materials and Manufacturing Research, The Ohio State University, Columbus, OH, 43210, USA. (ringel.5@osu.edu).

10.1109/JPHOTOV.2024.3463974 (accepted version)

layers [6], [7].

Several approaches to metamorphic epitaxial III-V/Si integration, such as using SiGe virtual substrates [8], [9], [10] and direct GaAs/Si growth followed by annealing and/or dislocation filter structures [11], [12], [13], have been explored over the years. While these methods have achieved impressive TDD values, the most promising approach that also allows full optical access to an underlying Si sub-cell, and which has given rise to the above-mentioned record cells, is through direct GaP growth on Si with a subsequent step-graded $GaAs_yP_{1-y}$ metamorphic buffer. Direct GaP/Si integration exploits the relatively small mismatch between the two materials, while the bandgap of each layer of the metamorphic $GaAs_yP_{1-y}$ stack is always greater than that of both the underlying Si *and* the terminal III-V top cell material, such as the $GaAs_{0.75}P_{0.25}$ used in current-matched dual-junction structures.

Following this III-V/GaP/Si approach, monolithic, all-epitaxial GaInP/AlGaAs/Si 3J cells have achieved certified AM1.5G efficiencies as high as 25.9% [14], whereas $GaAs_{0.75}P_{0.25}$/Si (2J) cells with the ideal 1.7 eV/1.1 eV 2J bandgap combination have reached certified efficiencies of 23.4% [15]; uncertified small area (0.123 cm^2) efficiencies of 25% have also been reported [16]. While lagging the performance of mechanically stacked and wafer bonded III-V/Si cells thus far, the combined promise of lower cost, large area scalability, and simpler device fabrication is compelling. Nonetheless, achieving higher efficiencies is largely dependent upon further TDD reduction.

Although years of work on this integration platform have indeed yielded substantial materials quality improvements, and have enabled the aforementioned record devices, the performance of cells fabricated using this approach are still significantly TDD-limited [14], [15], [16]. To reduce the deleterious effects of TDD in these cells we have focused on two parallel routes: (1) development of fundamental epitaxial processes and strategies for continued TDD reduction and (2) device design optimization that quantitatively accounts for the influence of TDD on minority carrier diffusion length (via non-radiative recombination) to yield improved defect tolerance.

With respect to TDD reduction, early efforts demonstrating processes for the nucleation of GaP on Si via both MBE and MOCVD were successful in yielding epilayers effectively free of antiphase domains [17], [18], [19], [20], [21]. However, the GaP layer itself was found to be a stubborn source of surprisingly high TDD, which the subsequent graded buffer was generally unable to reduce. For example, even for the aforementioned 23.4% GaAsP/Si tandem cell, the TDD within the GaP layer was $\sim 1\times10^7$ cm^{-2}, leading to similar TDD within the 1.7 eV $GaAs_{0.75}P_{0.25}$ top cell. However, ensuing work by multiple researchers toward an improved understanding of the dislocation dynamics within the heteroepitaxial GaP layer itself have served to inform several advances in the growth processes and associated dislocation-control strategies.

Extensive studies examining epitaxial growth conditions and doping, correlated with quantitative defect population and evolution analyses, revealed that the high TDD values were the result of very low dislocation glide velocities and nucleation layer instability in the GaP [22], [23], [24]. More recently, we have shown that by introducing a compressively strained GaAsP/GaP superlattice (CSS) embedded early in the growth structure the initially poor GaP dislocation glide dynamics can be enhanced, resulting in a remarkable TDD reduction within the fully relaxed GaP layer on Si from 1×10^7 cm^{-2} to 2×10^6 cm^{-2} [25]. Subsequent growth of step-graded $GaAs_yP_{1-y}$ metamorphic buffers out to the desired $GaAs_{0.75}P_{0.25}$ 2J top cell composition (3% lattice constant mismatch with respect to Si) successfully maintained this TDD value, and virtual $GaAs_{0.75}P_{0.25}$ substrates with a TDD of $\leq 3\times10^6$ cm^{-2} were demonstrated. At this TDD, GaAsP/Si tandem (2J) cells with significantly improved efficiency are expected.

In parallel to the TDD reduction work, multiple efforts have considered how to better optimize III-V cell design to account for higher-than-desired TDD values. The first-order approach is thickness optimization of both, the cell's base and emitter layers [26], [27]. Such adjustments, usually in the form of thinning, are applied to better match the real TDD-limited minority carrier diffusion length, minimizing recombination loss within the cell. To further improve the performance of these thinner layer designs, adequate photon management is needed, and the use of rear distributed Bragg reflectors [28], [29] and light trapping schemes [30] have been considered.

Of course, it is also possible to more drastically change the cell design. For example, to address the base width vs. diffusion length optimization, cells employing an n/i/p design have also been developed [7], [16]. However, while the increased depletion width of the n/i/p does improve carrier collection, it comes at the cost of voltage reduction. Another approach that has been effective for III-V cells on SiGe/Si substrates is to employ a p^+/n emitter/base cell configuration instead of the more common n^+/p design. This method exploits differences in electron and hole lifetimes and recombination rates that influence dark recombination current and thus V_{OC} [31], [32]. Nonetheless, for GaP/Si-based structures, the p^+/n configuration cannot be used due to the conduction and valence band offset energies that necessitate an n-GaP/n-Si heterojunction. This fundamental property effectively constrains monolithic III-V/Si cells to the n^+/p polarity. A rear-emitter design has been investigated for this application, but was found to have other debilitating limitations when the TDD was not already very low [33].

Ultimately, the highest performance cells will require both lower TDD and materials property informed design refinement. We describe herein work toward that end for 1.7 eV bandgap $GaAs_{0.75}P_{0.25}$ top cells, for application to $GaAs_{0.75}P_{0.25}$/Si tandems, employing the aforementioned low-TDD $GaAs_yP_{1-y}$/Si substrates coupled with an optimally-designed base doping gradient to reduce the remaining TDD-induced recombination loss. This new design was then found to fortuitously reveal additional long-wavelength carrier collection (J_{SC}) and associated V_{OC} losses related to the back surface field (BSF) that were previously masked by the TDD-induced losses, thereby guiding an update to the BSF that successfully

10.1109/JPHOTOV.2024.3463974 (accepted version)

recovered said losses. The resultant single-junction cells represent the highest-performance $GaAs_{0.75}P_{0.25}$-on-Si to date, with great promise for future implementation in a new generation of $GaAs_{0.75}P_{0.25}$/Si tandem solar cells.

II. Experimental Approach

All devices used in this study were grown via metal-organic chemical vapor deposition (MOCVD) using an Aixtron 3×2" close-coupled showerhead system. The reactor is equipped with an in-situ growth temperature and rate monitoring kSA ICE reflectance/pyrometry system. Precursors used for the group-III elements (Al, Ga, In) were trimethylaluminum (TMAl), trimethylgallium (TMGa), triethylgallium (TEGa), and trimethylindium (TMIn); precursors used for the group-V elements (As, P) were arsine (AsH_3), phosphine (PH_3), and tert-butylphosphine (TBP). N- and p-type dopant precursors used were silane (SiH_4) and diethylzinc (DEZn) within the cell and graded buffer and diethyltelluride (DETe) and bromotrichloromethane ($CBrCl_3$) within the tunnel junction layers, respectively.

Starting with 100 mm diameter, 350 µm thick, lightly p-type (TopSil, B-doped, 1-5 Ω-cm) float zone Si (001) wafers, with an intentional offcut of 2° toward [110], 50 nm GaP integration templates were grown on the Si substrates. A 3-period CSS consisting of n-$GaAs_{0.17}P_{0.83}$ / n-GaP layers was grown on the thin n-GaP/Si, followed by 450 nm thick GaP and subsequent $GaAs_yP_{1-y}$ step-graded buffer (SGB). A 1.0% μm^{-1} strain grading rate was employed in the SGB to accommodate the 3% total lattice mismatch, using 3.5% As fraction steps of equal thickness [25]. Next, a heterojunction tunnel diode consisting of 25 nm p^{++}-$Al_{0.2}Ga_{0.8}As_{0.75}P_{0.25}$ and 100 nm n^{++}-$GaAs_{0.75}P_{0.25}$, with nominal bandgaps of 2.0 eV and 1.7eV, respectively, was grown [34]. Finally, a $GaAs_{0.75}P_{0.25}$ (hereafter "GaAsP") solar cell, with 1.72 eV target bandgap and internally lattice-matched $Al_{0.64}In_{0.36}P$ and $Ga_{0.64}In_{0.36}P$ window and BSF layers, respectively, were grown. The full growth / device structure is schematically depicted in Fig. 1.

For the sake of relative simplicity, and because this work focused exclusively on the top cell, all growths performed for this study made use of as-received p-Si wafers with no bottom cell processing. Furthermore, because the n-GaP / p-Si interface would have served as a second junction, backside contact to the GaAsP cell was made using the SGB as a lateral conduction layer (LCL) contact, isolating the active test region to just the combined GaAsP top cell and tunnel junction structure; note that the LCL was expected to contribute additional series resistance and a small associated fill factor loss. Device fabrication involved mesa isolation and LCL reveal using a BCl_3/Ar-based inductively couple plasma etch. Electron beam evaporated Ni/GeAu n-type metal contacts were used for both the top grid and large area LCL back contacts. No anti-reflection coatings were applied to the cells reported here.

An array of square 4 mm^2 cells were characterized by internal quantum efficiency (IQE), illuminated current-voltage (LIV), and J_{SC}-V_{OC} measurements. IQE measurements were performed using a custom small-spot, microscope-based system. LIV

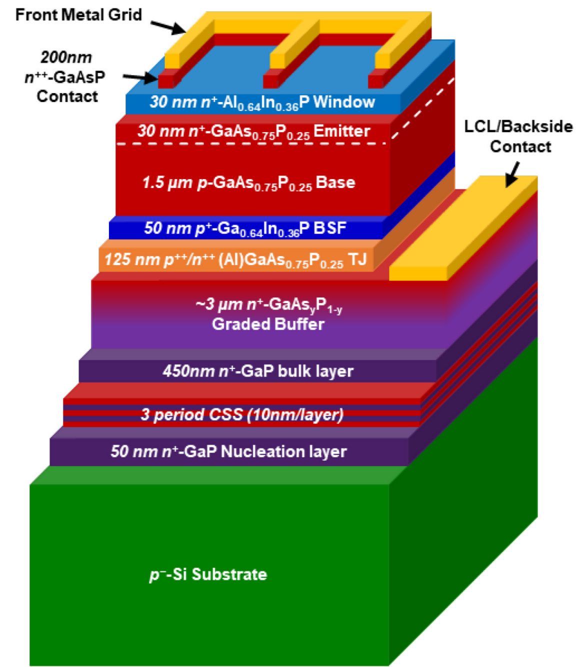

Fig. 1. Device schematic (not to scale) of the $GaAs_{0.75}P_{0.25}$ top cell grown on a Si substrate.

measurements were performed under a simulated AM1.5G spectrum using a TS Space Systems Unisim Compact two-zone (with four LED boost zones) solar simulator calibrated using multiple reference III-V and Si cells with different spectral responses. J_{SC}-V_{OC} was performed using a tunable high-power white LED with five orders of magnitude dynamic range. Measurement of voltage dependent collection was performed using the IQE stage with some modifications and will be detailed later. Electron channel contrast imaging (ECCI), performed in a Thermo Scientific Quattro scanning electron microscope fitted with a concentric backscatter detector, was used to determine reported TDD values using our previously established methods [35], [36], [37]. Reported cells are representative of their populations. All devices from this work can be referenced in Table I and samples will be introduced as relevant in the text.

III. Results And Discussion

A. Initial Results on Low-TDD GaAsP/Si Virtual Substrates

Use of the new low-TDD $GaAs_yP_{1-y}$/Si virtual substrates described above was expected to provide significantly improved minority carrier transport properties (lifetime and diffusion length) and solar cell performance metrics within the 1.7 eV $GaAs_{0.75}P_{0.25}$. Actual TDD, as measured via ECCI, of the cells presented here was 4.1 ± 0.5 $\times 10^6$ cm^{-2}. This is slightly higher than the initial virtual substrates, most likely due to some small compositional variances in the different cell layers. Nonetheless, this is still a significant reduction compared to the TDD of ~1×10^7 cm^{-2} in the prior GaAsP top cell within the aforementioned 23.4% tandem device [15].

Both the prior top cell (hereafter referred to as "top cell A," or TC-A) and the new version being investigated here (hereafter

10.1109/JPHOTOV.2024.3463974 (accepted version)

Table I. Tabulated cell metrics comparing the different GaAsP top cells. The small bandgap differences between the different cells makes direct comparison less meaningful, thus cell metrics are adjusted as noted in the text. Champion devices (bold) are shown alongside the mean with standard error (in parentheses) taken from a population of six solar cells, with the exception of the tandem (TC-A), which was taken from a separate study. [A] TC-A has an ARC. [B] Statistics available only from 3 cells.

ID	Description	*TDD* [cm^{-2}]	E_g [eV]	*Raw* V_{OC} [V]	W_{OC} [V]	*Raw Jsc* [mA/cm^2]	J_{IQE} [mA/cm^2]	*FF* [%]
TC-A	GaAsP-on-Si (*23.4% tandem*)	$1.4 \pm 0.1 \times 10^7$	1.67	1.11	0.56	17.1 [A]	17.5	77.7
TC-B	GaAsP-on-Si (*constant doping, GaInP BSF*)	$4.1 \pm 0.5 \times 10^6$	1.69	1.17 (1.17 ± 0.003)	0.52 (0.53 ± 0.003)	14.1 (13.9 ± 0.05)	18.4 (18.4 ± 0.13) [B]	78.3 (77.4 ± 0.36)
TC-C	GaAsP-on-Si (*graded doping, GaInP BSF*)	$3.8 \pm 1.2 \times 10^6$	1.72	1.19 (1.19 ± 0.002)	0.52 (0.53 ± 0.003)	14.2 (14.2 ± 0.02)	18.7 (18.8 ± 0.10) [B]	81.0 (81.0 ± 0.14)
TC-D	GaAsP-on-Si *(graded doping, AlGaAsP BSF)*	$6.3 \pm 0.2 \times 10^6$	1.72	1.27 (1.25 ± 0.006)	0.44 (0.47 ± 0.006)	14.0 (13.8 ± 0.08)	19.4 (19.4 ± 0.06)	81.0 (80.2 ± 0.22)
TC-R	GaAsP-on-GaAs *(constant doping, GaInP BSF)*	$1.5 \pm 0.3 \times 10^6$	1.74	1.28 (1.28 ± 0.001)	0.46 (0.46 ± 0.001)	13.8 (13.7 ± 0.09)	19.1 (19.2 ± 0.15) [B]	85.5 (85.0 ± 0.27)

referred to as "top cell B," or TC-B) were grown and fabricated in nominally identical processes, with two minor exceptions. First, a small and unintentional difference in composition, yielding bandgaps (via fitting of IQE) of 1.67 eV and 1.69 eV for TC-A and TC-B, respectively; the result of this discrepancy is a 10 nm longer absorption edge cutoff for TC-A. Second, a slightly thicker (30 nm vs. 20 nm) and higher doped (5×10^{18} cm^{-3} vs. 1×10^{18} cm^{-3}) $Al_{0.64}In_{0.36}P$ window layer in TC-B, commensurate with the authors' improved understanding of the associated design sensitivity for optimizing frontside passivation [38].

To account for the small bandgap discrepancies between these cells and all others compared in this work, a correction to IQE was applied by simply shifting the optical constants (n and k) to those of the target bandgap of 1.72 eV, using a Hovel model [39], [40] following formalizations from [41] and employing a transfer matrix model [42], [43] for more accurate simulation of internal reflections as established in [28], to reconstruct the IQE curves (shown in Fig. 2), and then re-integrating over the AM1.5G spectrum. Furthermore, the window layers were modeled to be 30nm in all cases to remove any window effects. Thus for a more accurate comparison of current between samples, the bandgap and window thickness adjusted total integrated current (from IQE, or J_{IQE}) will be used as the main metric. After accounting for these differences, the improvement in material quality was indeed found to translate into improved device performance. Compared to TC-A, IQE of TC-B is higher overall, with a total adjusted-J_{IQE} difference of 0.9 mA/cm^2, as tabulated in Table I. Comparing the two curves, shown in Fig. 2, it is clear that most of the improvement can be attributed to increased carrier collection towards longer wavelengths starting at around 480 nm. This improved behavior is consistent with reduced TDD in TC-B, as the expected increase in minority carrier diffusion length commensurately increases the probability of collecting photogenerated carriers from deeper within the base (i.e., further away from depletion region drift field).

In our previous report of the 23.4% efficient tandem cell,

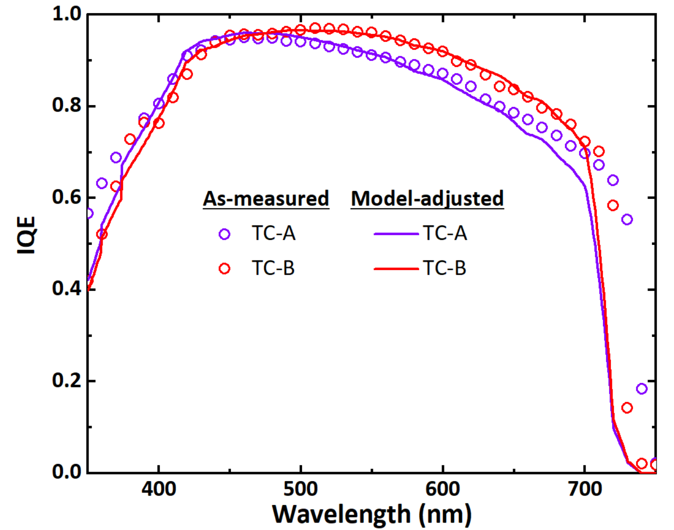

Fig. 2. Internal quantum efficiency of TC-A (TDD = 1×10^7 cm^{-2}) and TC-B (TDD = 4.1×10^6 cm^{-2}) as-measured (open circles) vs. as-adjusted for accurate comparison via modeling (solid lines).

extensive loss analysis of the top cell revealed that the FF was reduced due to voltage dependent collection (VDC) caused by subpar minority carrier diffusion length [15]. To investigate whether VDC loss in the lower-TDD cells is commensurately improved we have performed a similar analysis here. $F_{VDC}(\lambda)$ is a parameter developed to quantify the fraction of photocurrent lost per volt as a function of wavelength, enabling a more direct comparison between the single-junction GaAsP cells and the two junction 23.4% cell. We note that while $F_{VDC}(\lambda)$ analysis provides similar insight as voltage-dependent IQE, it has two major advantages of the latter: yields higher precision characterization of voltage-affected photocurrent due to the use of finer voltage steps than typically done for voltage-dependent IQE and is a more direct measure of the LIV curve "flat" region slope. Although this technique is described in detail in [15], as it is a newer method, we briefly explain it below.

In the absence of any discernable impact of finite shunt

10.1109/JPHOTOV.2024.3463974 (accepted version)

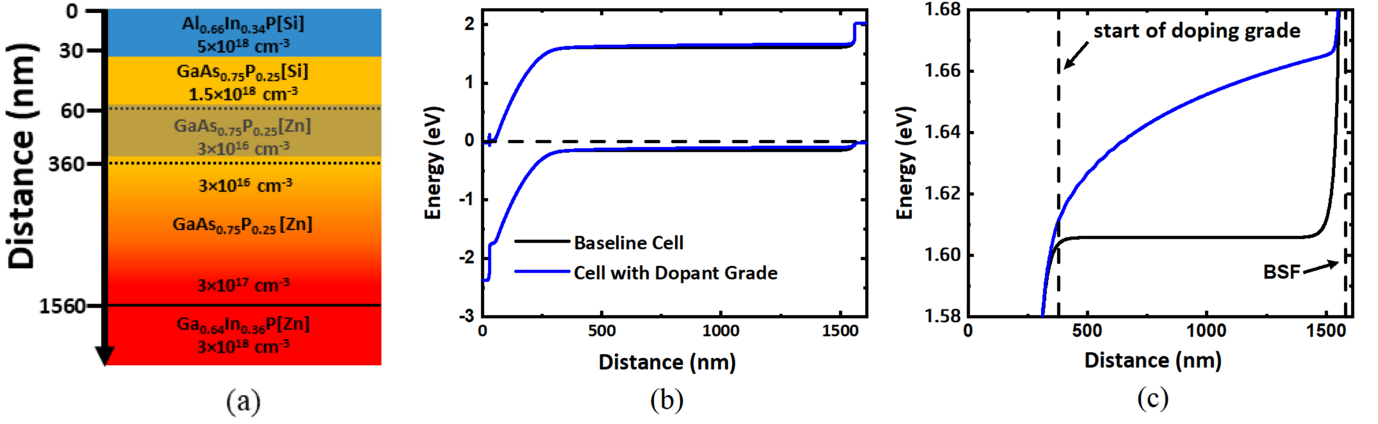

Fig. 4. (a) Structure of the cell with a dopant grade (not to scale). The grey area denotes the depletion region. (b) Energy band diagram of the base of a GaAsP top cell with and without a base dopant grade. (c) Zoomed in profile of the conduction band energy of the two cells, highlighting the increased band-bending as a result of the dopant grade.

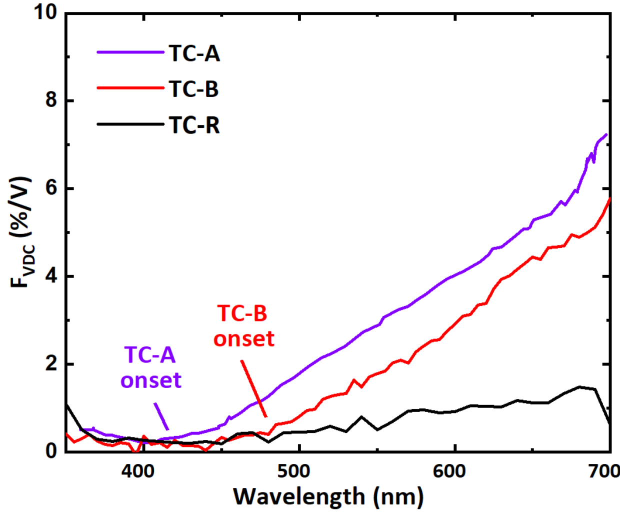

Fig. 3. Spectrally resolved voltage dependent collection measurement comparing GaAsP top cells with different TDDs.

resistance, $F_{VDC}(\lambda)$ is defined, for each monochromatic wavelength step, as the slope of the illuminated I-V curve at J(V≈0), normalized to the short circuit current density:

$$F_{VDC}(\lambda) \equiv \frac{\left[\frac{dJ(\lambda,V\approx 0)}{dV}\right]}{J(\lambda,V\approx 0)}. \quad (1)$$

Thus, an F_{VDC} parameter of zero would indicate no measured VDC effects. The slope of the LIV curve can be analytically described with its EQE and F_{VDC} by integrating over the illumination spectrum (AM1.5G) and rearranging (1):

$$\frac{dJ(\lambda,V\approx 0)}{dV} = \int_{\lambda=min}^{max} EQE(\lambda)\cdot\Phi_{AM1.5G}(\lambda)\cdot F_{VDC}(\lambda)\cdot d\lambda. \quad (2)$$

As shown in Fig. 3, the lower TDD (4.1×10^{6} cm^{-2}) in TC-B improved (reduced) the F_{VDC} factor across all wavelengths versus TC-A (TDD ~ 1×10^{7} cm^{-2}), consistent with the expected improvement in diffusion length. In line with this result, the onset of non-zero F_{VDC} in TC-B was also improved (delayed) by about 50 nm, from ~400 nm to ~450 nm, indicating that VDC effects are beginning deeper in the base. To serve as an even lower-TDD reference, nominally identical GaAsP cells were also grown on a relaxed tensile-graded $GaAs_yP_{1-y}$ buffer on a GaAs substrate, hereafter referred to TC-R. The low (1.5×10^{6} cm^{-2}) TDD of this cell effectively serves as a high-quality benchmark target, or reference, for GaAsP/Si development, as detailed in [44]. While TC-B is significantly improved compared with TC-A, it is also clear from TC-R that further TDD reduction is still needed. More importantly, the still sizeable difference between the TC-B and TC-R F_{VDC} profiles highlight the high degree of sensitivity for carrier losses that still exist in the 1 – 4×10^{6} cm^{-2} TDD range.

B. Design Improvements on low-TDD GaAsP/Si platform

To at least partially mitigate the voltage dependent collection issue in lieu of further TDD reduction, a graded dopant profile [45], [46] was implemented within the base. The intent of this design element was to introduce a small, but non-negligible electric (drift) field extending through the entire base region of the cell to help enhance carrier collection. Unlike n-i-p device designs, which also create an extended drift field, the dopant grade should do so without significantly increasing the depletion region volume, thereby avoiding the J_{02} based V_{OC} reduction reported for n-i-p GaAsP cells [16]. Therefore, the dopant gradient induced field is expected to improve the relative defect tolerance of the cell at low-to-mid TDD values without adversely impacting the V_{OC}.

As depicted in Fig. 4(a), the new base design consisted of a 300 nm region at a nominally constant doping level of 3×10^{16} cm^{-3} to effectively "encapsulate" the junction depletion region (calculated to be 280 nm at zero bias) below the emitter, with the remaining 1200 nm base extension to the back surface field (BSF) layer consisting of a linear dopant grade from 3×10^{16} cm^{-3} to 3×10^{17} cm^{-3}, ending at the 3×10^{18} cm^{-3} doped GaInP BSF. This was achieved using a proportional grade of the DeZn precursor flow during MOCVD growth, based on several individual doping calibration growths. A simple simulation using the BandEng program [47] was used to help quantify the resultant band bending within the graded dopant cell, presented

10.1109/JPHOTOV.2024.3463974 (accepted version)

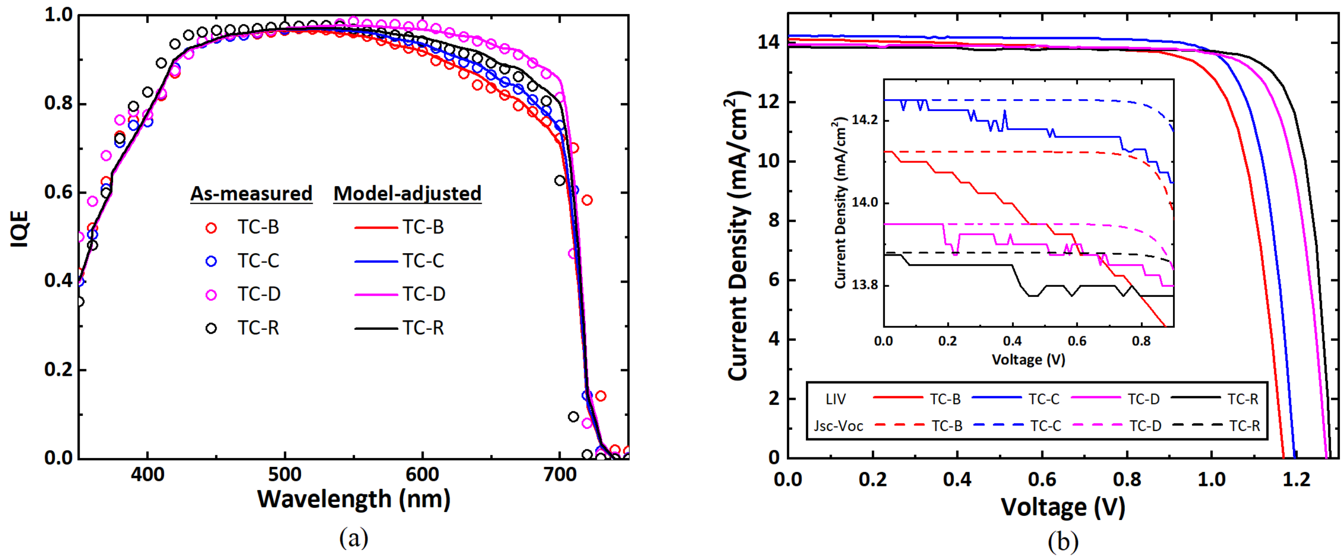

Fig. 5. (a) Internal quantum efficiency as-measured (open circles) vs model-adjusted (solid lines). (b) LIV of the different top cells and in the inset of (b) is zoomed in LIV (solid lines) and J_{SC}-V_{OC} (dashed lines) of the different top cells, showing the VDC reduction.

in Fig. 4(b,c). Following the nomenclature above, as introduced in Table I, where TC-A refers to the TDD = 1×10^7 cm^{-2} top cell from the 23.4% tandem cell and TC-B refers to the reduced-TDD (4.1×10^6 cm^{-2}) top cell produced using the CSS structure, the new cell implementing the grading dopant profile is referred to as TC-C. Aside from the doping gradient, TC-C was otherwise identical to TC-B, and possessed an effectively equal TDD of $3.8 \pm 1.2 \times10^6$ cm^{-2}.

Subsequently, changes were also made to the BSF, swapping the nominally lattice-matched, highly-doped p^+-$Ga_{0.66}In_{0.34}P$ BSF to a p^+-$Al_{0.2}Ga_{0.8}As_{0.74}P_{0.26}$ analogue, following work that demonstrated improved minority carrier lifetime in similar devices [16], possibly due to a simpler growth of an In-free, base/BSF heterointerface and a more favorable band offset. This cell is hereafter referred to as TC-D and is otherwise identical in design to TC-C except for the updated BSF. The TDD (6.3×10^6 cm^{-2}) of TC-D was actually slightly higher than TC-C, but still substantially lower than TC-A. Nonetheless, despite the higher TDD, TC-D was still found to provide further improvement over TC-C, confirming the importance of a quality base/BSF interface.

Fig. 5 presents IQE and LIV comparing the design changes from TC-B through TC-D, referenced against TC-R, while Fig. 6 shows a statistical summary of the improvements from multiple cells. As noted previously with Fig. 3, Fig. 5(a) employs the same fitting of experimental results to a Hovel model in order to normalize any differences, particularly in bandgap between samples. Thus, to fully interpret the results shown in both Figs. 5(a) and 5(b), metrics such as the E_g-V_{OC} offset (W_{OC}) and model-adjusted J_{IQE} values were extracted and are listed in Table I, alongside FF and TDD values for reference. After adjusting for the difference in bandgap between the two cells, there is a +0.3 mA/cm^2 total improvement in J_{IQE} between TC-B and TC-C. As seen in Fig. 5(a), the increased for TC-C in the long-wavelength region (>550 nm) clearly

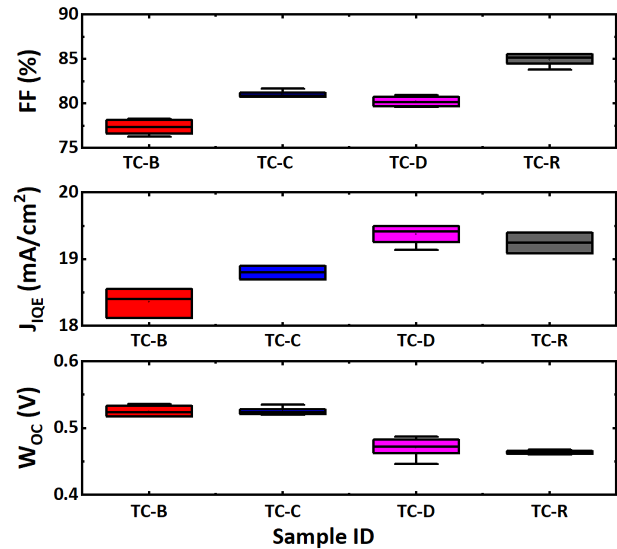

Fig. 6 Box and whisker plots (25th and 75th percentile) comparing the key metrics of improvement for the different GaAsP top cell designs.

indicates that this J_{SC} improvement is a direct outcome of the dopant grade. When combined with the BSF changes the J_{SC} improvement is even more dramatic, yielding a +1.0 mA/cm^2 difference versus TC-B. What is particularly notable about this result is that it actually surpasses the J_{IQE} of the ~4× lower TDD benchmark TC-R cell.

The inset of Fig. 5(b) focuses on the LIV curves in the 0.0 – 0.9 V range, comparing them to pseudo-LIV curves produced via 1-sun shifted J_{SC}-V_{OC} measurements; this latter measurement effectively removes the effect of VDC because the data is taken only at the J_{SC} and V_{OC} points under varying illumination intensities [48], [49]. The deviation of the real LIV curves from the pseudo-LIV curves thus serves as another measure of VDC. The values of the negative slope in the LIV curves (via linear fitting from 0.0 – 0.5 V) are tabulated in Table

10.1109/JPHOTOV.2024.3463974 (accepted version)

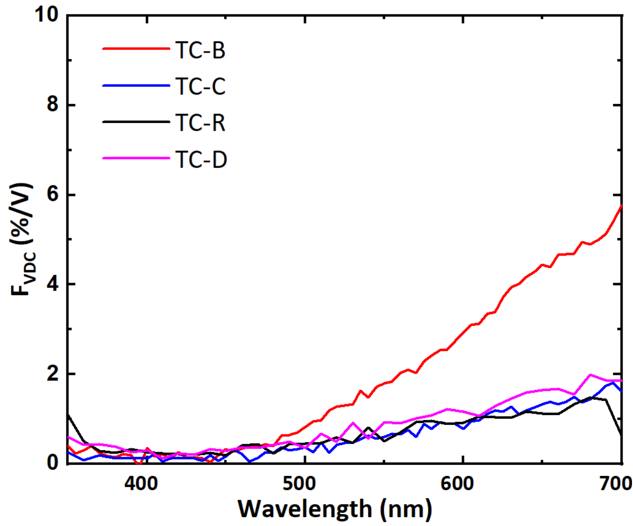

Fig. 7. Spectrally resolved voltage dependent collection efficiency measurement comparing the top cells. The constant base doping (TC-B) displays much higher F_{VDC} than all other top cells.

II. The TC-C, TC-D, and TC-R cells exhibit nearly identical slopes, which is in stark contrast to the ~2.5× steeper slope of TC-B, highlighting the significantly reduced (i.e. improved) VDC afforded by the dopant grade within TC-C and TC-D. This improved LIV slope corresponded to an increase in FF of 2.7% absolute for both cells, achieved without any practical TDD reduction between TC-B and TC-C, and in fact an increase for TC-D.

F_{VDC} measurements, presented in Fig. 7, clearly confirm that the dopant grade was successful in bridging the gap in VDC between the benchmark TC-R cell and the constant base doping TC-B cell on Si. In fact, the F_{VDC} profile of both TC-C and TC-D are near perfect matches to TC-R, which has much lower TDD (1.5x10^6 cm^{-2}). Using (2), the F_{VDC} measurements can predict the slope of the LIV measurements, as tabulated in Table II; these values align well with the measured results from Fig. 5(b), clearly demonstrating substantial improvement in defect tolerance. To completely remove all VDC effects, TDD reduction below 1×10^6 cm^{-2} would be necessary [31], as well as extensive growth optimization to minimize all point defects. It is also worth noting here that, as opposed to TC-A and TC-R, which both made use of proper, large-area wafer backside contacts, TC-B, TC-C, and TC-D all used LCL structures that introduce extra series resistance and associated FF reduction; we estimate as much as 1.6% absolute FF reduction to be present here [50].

Finally, the E_g-V_{OC} offset (W_{OC}) was found to remain constant at ~0.52 V between TC-B and TC-C, indicating that there was indeed no major voltage loss arising from the dopant grade, unlike that typically observed in n-i-p designs [51]. IQE modeling using the expected TDD-limited diffusion length estimates from the Yamaguchi model [52] did not match the measured long-wavelength collection. For TC-B, the minority carrier diffusion length in the base was well fitted by the estimated TDD-derived diffusion length [15]. However, the

Table II. Tabulated negative slope from LIV compared to the predicted values calculated from $\mathbf{F_{VDC}}$ measurement of the different cells. The significantly reduced slope of TC-C and TC-D highlights the associated reduced VDC afforded by the dopant grade compared to TC-B.

ID	Description	*TDD* [cm^{-2}]	*LIV Slope* [mA/V-cm^2]	*F_{VDC} Slope* [mA/V-cm^2]
TC-B	GaAsP-on-Si (*constant doping, GaInP BSF*)	4.1×10^6	0.35	0.34
TC-C	GaAsP-on-Si (*graded doping, GaInP BSF*)	3.8×10^6	0.14	0.11
TC-D	GaAsP-on-Si *(graded doping, AlGaAsP BSF)*	6.3×10^6	0.14	0.11
TC-R	GaAsP-on-GaAs (*constant doping, GaInP BSF*)	1.5×10^6	0.15	0.18

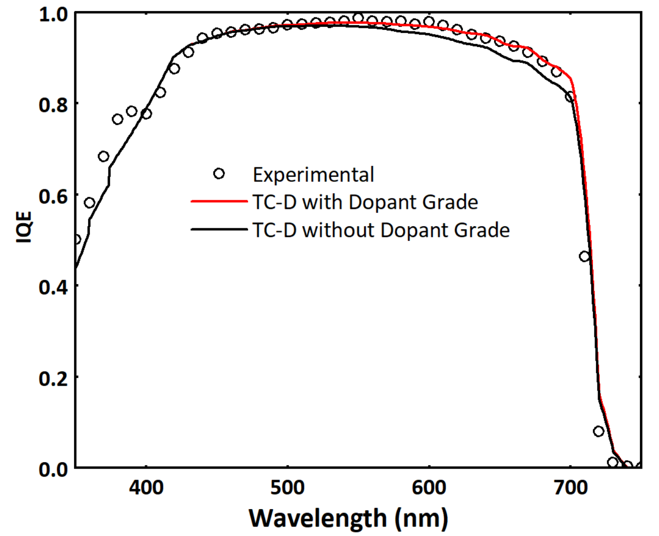

Fig. 8 Internal quantum efficiency as-measured (open circles) vs model-adjusted (solid lines) of TC-D comparing the difference in long-wavelength collection with and without a dopant grade.

improved collection provided by the dopant grade appears to have revealed additional losses that were most likely previously masked by the excess TDD; for example, a relatively high recombination velocity at the base/BSF interface. Indeed, both the W_{OC} and the IQE behavior was greatly improved with the addition of the AlGaAsP BSF in TC-D.

To deconvolve the impacts of the dopant grade and replaced BSF within TC-D, modeling following the same techniques as described previously for Fig. 3 and Fig. 5(a) was employed. Fig. 8 compares the expected IQE of TC-D at the measured TDD, both with and without any doping grade induced electric field enhancements. Within the experimentally-informed model of all samples, the best fit for the base/BSF IRV was found to be between 6×10^4 and 5×10^5 cm/s, except TC-D which was best fit using a very low IRV value of 500 cm/s. However, even assuming no IRV at the interface, the long-wavelength IQE could not be properly fit to the experimental data without the addition of an electric field enhancement. Furthermore, the J_{IQE} of TC-D modeled without the dopant grade is 19.1 mA/cm^2

10.1109/JPHOTOV.2024.3463974 (accepted version)

while the TC-D J_{IQE} is 19.4 mA/cm^2, perfectly aligning with the 0.3mA/cm^2 difference in J_{IQE} between TC-B and TC-C, proving the effectiveness of the dopant grade goes beyond simply repelling carriers from recombination at the base/BSF interface and indeed mitigates TDD-induced recombination.

IV. Conclusion

Advances in GaP/Si integration and subsequent $GaAs_yP_{1-y}$ metamorphic structures enabled the growth of 1.7 eV single junction $GaAs_{0.75}P_{0.25}$ top cells at a TDD of 4×10^6 cm^{-2}. However, even at relatively low TDD, VDC and poor long-wavelength collection were still found to be major performance limiters. By implementing a carefully tailored base doping gradient, both the J_{SC} and FF were significantly increased, by ~0.3 mA/cm^2 and 2.7% absolute, respectively, without reduction in V_{OC}, at the same TDD. Furthermore, this design revealed the deleterious role of a non-ideal base/BSF, which was addressed via an updated BSF design. The new BSF, coupled with the dopant grade, yielded a $GaAs_{0.75}P_{0.25}$ cell on Si with a TDD of 6.3×10^6 cm^{-2} that surpasses the J_{SC} and W_{OC} of a prior-design reference cell with ~4× lower TDD. This work not only demonstrates a high performance GaAsP-on-Si top cell ready for implementation in a GaAsP/Si tandem, but also presents a simple and effective strategy to significantly improve defect tolerance for metamorphic III-V solar cells.

References

[1] M.A. Green, *et al.*, " Solar cell efficiency tables (Version 64)," *Progress in Photovoltaics: Research and Applications*, vol. 32, no. 7, p. 425, July 2024; doi: 10.1002/pip.3831.

[2] C. Algora, “Reliability of III–V concentrator solar cells,” *Microelectronics Reliability*, vol. 50, no. 9–11, pp. 1193–1198, Sep. 2010, doi: 10.1016/j.microrel.2010.07.045.

[3] M. Vázquez, C. Algora, I. Rey-Stolle, and J. R. González, “III-V concentrator solar cell reliability prediction based on quantitative LED reliability data,” *Progress in Photovoltaics: Research and Applications*, vol. 15, no. 6, pp. 477–491, 2007, doi: 10.1002/pip.753.

[4] S. Essig *et al.*, “Raising the one-sun conversion efficiency of III–V/Si solar cells to 32.8% for two junctions and 35.9% for three junctions,” *Nat Energy*, vol. 2, no. 9, p. 17144, Aug. 2017, doi: 10.1038/nenergy.2017.144.

[5] P. Schygulla *et al.*, “Two-terminal III–V//Si triple-junction solar cell with power conversion efficiency of 35.9 % at AM1.5g,” *Progress in Photovoltaics: Research and Applications*, vol. 30, no. 8, pp. 869–879, 2022, doi: 10.1002/pip.3503.

[6] M. J. Mori, S. T. Boles, and E. A. Fitzgerald, “Comparison of compressive and tensile relaxed composition-graded GaAsP and (Al)InGaP substrates,” *Journal of Vacuum Science & Technology A: Vacuum, Surfaces, and Films*, vol. 28, no. 2, pp. 182–188, Mar. 2010, doi: 10.1116/1.3290762.

[7] S. Fan *et al.*, “Effects of Graded Buffer Design and Active Region Structure on GaAsP Single-Junction Solar Cells Grown on GaP/Si Templates,” in *2020 47th IEEE Photovoltaic Specialists Conference (PVSC)*, Jun. 2020, pp. 2044–2046. doi: 10.1109/PVSC45281.2020.9300775.

[8] M. R. Lueck, C. L. Andre, A. J. Pitera, M. L. Lee, E. A. Fitzgerald, and S. A. Ringel, “Dual junction GaInP/GaAs solar cells grown on metamorphic SiGe/Si substrates with high open circuit voltage,” *IEEE Electron Device Letters*, vol. 27, no. 3, pp. 142–144, Mar. 2006, doi: 10.1109/LED.2006.870250.

[9] M. Diaz *et al.*, “Tandem GaAsP/SiGe on Si solar cells,” *Solar Energy Materials and Solar Cells*, vol. 143, pp. 113–119, Dec. 2015, doi: 10.1016/j.solmat.2015.06.033.

[10] J. A. Carlin *et al.*, “III-V Device Integration on Silicon Via Metamorphic SiGe Substrates,” *ECS Trans.*, vol. 3, no. 7, pp. 729–743, Oct. 2006, doi: 10.1149/1.2355868.

[11] M. Yamaguchi, C. Amano, and Y. Itoh, “Numerical analysis for high-efficiency GaAs solar cells fabricated on Si substrates,” *Journal of Applied Physics*, vol. 66, no. 2, pp. 915–919, Jul. 1989, doi: 10.1063/1.343520.

[12] R. K. Ahrenkiel *et al.*, “Minority Carrier Lifetime of GaAs on Silicon,” *J. Electrochem. Soc.*, vol. 137, no. 3, 1990.

[13] C. Shang *et al.*, “A Pathway to Thin GaAs Virtual Substrate on On-Axis Si (001) with Ultralow Threading Dislocation Density,” *physica status solidi (a)*, vol. 218, no. 3, p. 2000402, 2021, doi: 10.1002/pssa.202000402.

[14] M. Feifel *et al.*, “Epitaxial GaInP/GaAs/Si Triple-Junction Solar Cell with 25.9% AM1.5g Efficiency Enabled by Transparent Metamorphic AlxGa1−xAsyP1−y Step-Graded Buffer Structures,” *Solar RRL*, vol. 5, no. 5, p. 2000763, 2021, doi: 10.1002/solr.202000763.

[15] D. L. Lepkowski *et al.*, “23.4% monolithic epitaxial GaAsP/Si tandem solar cells and quantification of losses from threading dislocations,” *Solar Energy Materials and Solar Cells*, vol. 230, p. 111299, Sep. 2021, doi: 10.1016/j.solmat.2021.111299.

[16] S. Fan *et al.*, “Current-Matched III–V/Si Epitaxial Tandem Solar Cells with 25.0% Efficiency,” *Cell Reports Physical Science*, vol. 1, no. 9, p. 100208, Sep. 2020, doi: 10.1016/j.xcrp.2020.100208.

[17] Y. Takagi, H. Yonezu, K. Samonji, T. Tsuji, and N. Ohshima, “Generation and suppression process of crystalline defects in GaP layers grown on misoriented Si(1 0 0) substrates,” *Journal of Crystal Growth*, vol. 187, no. 1, pp. 42–50, Apr. 1998, doi: 10.1016/S0022-0248(97)00862-2.

[18] T. J. Grassman *et al.*, “Control and elimination of nucleation-related defects in GaP/Si(001) heteroepitaxy,” *Appl. Phys. Lett.*, vol. 94, no. 23, p. 232106, Jun. 2009, doi: 10.1063/1.3154548.

[19] K. Volz *et al.*, “GaP-nucleation on exact Si (001) substrates for III/V device integration,” *Journal of Crystal Growth*, vol. 315, no. 1, pp. 37–47, Jan. 2011, doi: 10.1016/j.jcrysgro.2010.10.036.

[20] T. J. Grassman *et al.*, “Nucleation-related defect-free GaP/Si(100) heteroepitaxy via metal-organic chemical vapor deposition,” *Appl. Phys. Lett.*, vol. 102, no. 14, p. 142102, Apr. 2013, doi: 10.1063/1.4801498.

[21] E. L. Warren, A. E. Kibbler, R. M. France, A. G. Norman, P. Stradins, and W. E. McMahon, “Growth of antiphase-domain-free GaP on Si substrates by metalorganic chemical vapor deposition using an *in situ* AsH $_3$ surface preparation,” *Appl. Phys. Lett.*, vol. 107, no. 8, p. 082109, Aug. 2015, doi: 10.1063/1.4929714.

[22] J. T. Boyer, A. N. Blumer, Z. H. Blumer, D. L. Lepkowski, and T. J. Grassman, “Correlation of early-stage growth process conditions with dislocation evolution in MOCVD-based GaP/Si heteroepitaxy,” *Journal of Crystal Growth*, vol. 571, p. 126251, Oct. 2021, doi: 10.1016/j.jcrysgro.2021.126251.

[23] R. D. Hool *et al.*, “Challenges of relaxed *n* -type GaP on Si and strategies to enable low threading dislocation density,” *Journal of Applied Physics*, vol. 130, no. 24, p. 243104, Dec. 2021, doi: 10.1063/5.0073525.

[24] M. Nandy *et al.*, “Reduction of defects in GaP layers grown on Si(100) by MOCVD,” in *2021 IEEE 48th Photovoltaic Specialists Conference (PVSC)*, Jun. 2021, pp. 1344–1347. doi: 10.1109/PVSC43889.2021.9518758.

[25] J. T. Boyer, A. N. Blumer, Z. H. Blumer, D. L. Lepkowski, and T. J. Grassman, “Reduced Dislocation Introduction in III–V/Si Heterostructures with Glide-Enhancing Compressively Strained Superlattices,” *Crystal Growth & Design*, vol. 20, no. 10, pp. 6939–6946, Oct. 2020, doi: 10.1021/acs.cgd.0c00992.

[26] A. C. Silvaggio, D. L. Lepkowski, D. J. Chmielewski, J. T. Boyer, S. A. Ringel, and T. J. Grassman, “Optimization of a GaAsP Top Cell for Implementation in a III-V/Si Tandem Structure,” in *2017 IEEE 44th Photovoltaic Specialist Conference (PVSC)*, Jun. 2017, pp. 2554–2557. doi: 10.1109/PVSC.2017.8366475.

[27] M. Vaisman *et al.*, “15.3%-Efficient GaAsP Solar Cells on GaP/Si Templates,” *ACS Energy Lett.*, vol. 2, no. 8, pp. 1911–1918, Aug. 2017, doi: 10.1021/acsenergylett.7b00538.

[28] D. L. Lepkowski, T. Kasher, T. J. Grassman, and S. A. Ringel, “Designing an Epitaxially-Integrated DBR for Dislocation Mitigation in Monolithic GaAsP/Si Tandem Solar Cells,” *IEEE Journal of Photovoltaics*, vol. 11, no. 2, pp. 400–407, Mar. 2021, doi: 10.1109/JPHOTOV.2020.3043105.

[29] R. M. France *et al.*, “Graded buffer Bragg reflectors with high reflectivity and transparency for metamorphic optoelectronics,” *Journal*

of Applied Physics, vol. 129, no. 17, p. 173102, May 2021, doi: 10.1063/5.0050588.

[30] S. Fan *et al.*, *Epitaxial GaAsP/Si Tandem Solar Cells with Integrated Light Trapping*. 2019, p. 0733. doi: 10.1109/PVSC40753.2019.8980664.

[31] C. L. Andre, D. M. Wilt, A. J. Pitera, M. L. Lee, E. A. Fitzgerald, and S. A. Ringel, "Impact of dislocation densities on n+/p and p+/n junction GaAs diodes and solar cells on SiGe virtual substrates," *Journal of Applied Physics*, vol. 98, no. 1, p. 014502, Jul. 2005, doi: 10.1063/1.1946194.

[32] S. Fan, D. Jung, Y. Sun, B. D. Li, D. Martin-Martin, and M. L. Lee, "16.8%-Efficient n $^+$ /p GaAs Solar Cells on Si With High Short-Circuit Current Density," *IEEE J. Photovoltaics*, vol. 9, no. 3, pp. 660–665, May 2019, doi: 10.1109/JPHOTOV.2019.2894657.

[33] D. L. Lepkowski, J. T. Boyer, D. J. Chmielewski, A. C. Silvaggio, S. A. Ringel, and T. J. Grassman, "Investigation of Rear-Emitter GaAs0.75P0.25 Top Cells for Application to III–V/Si Tandem Photovoltaics," *IEEE Journal of Photovoltaics*, vol. 9, no. 6, pp. 1644–1651, Nov. 2019, doi: 10.1109/JPHOTOV.2019.2939069.

[34] D. J. Chmielewski, D. L. Lepkowski, J. T. Boyer, T. J. Grassman, and S. A. Ringel, "Metamorphic Tunnel Junctions Grown Via MOCVD Designed for GaAs0.75P0.25/Si Tandem Solar Cells," *IEEE Journal of Photovoltaics*, vol. 11, no. 2, pp. 408–414, Mar. 2021, doi: 10.1109/JPHOTOV.2021.3052773.

[35] S. D. Carnevale *et al.*, "Rapid misfit dislocation characterization in heteroepitaxial III-V/Si thin films by electron channeling contrast imaging," *Appl. Phys. Lett.*, vol. 104, no. 23, p. 232111, Jun. 2014, doi: 10.1063/1.4883371.

[36] S. D. Carnevale *et al.*, "Applications of Electron Channeling Contrast Imaging for the Rapid Characterization of Extended Defects in III–V/Si Heterostructures," *IEEE Journal of Photovoltaics*, vol. 5, no. 2, pp. 676–682, Mar. 2015, doi: 10.1109/JPHOTOV.2014.2379111.

[37] J. I. Deitz, S. D. Carnevale, S. A. Ringel, D. W. McComb, and T. J. Grassman, "Electron Channeling Contrast Imaging for Rapid III-V Heteroepitaxial Characterization," *J Vis Exp*. (101), e52745, Jul. 2015, doi: 10.3791/52745.

[38] D. L. Lepkowski, T. Kasher, J. T. Boyer, D. J. Chmielewski, T. J. Grassman, and S. A. Ringel, "The Critical Role of AlInP Window Design in III–V Rear-Emitter Solar Cells," *IEEE Journal of Photovoltaics*, vol. 10, no. 3, pp. 758–764, May 2020, doi: 10.1109/JPHOTOV.2020.2978863.

[39] H. J. Hovel, "The effect of depletion region recombination currents on the efficiencies of Si and GaAs solar cells.," presented at the Photovoltaic Specialists Conference, Palo Alto, California: IEEE, 1974, pp. 34–39.

[40] H. J. Hovel, Ed., *Semiconductors and semimetals. 11: Solar cells / ed. by Harold J. Hovel*, 4. print. 1983.

[41] M. P. Lumb *et al.*, "Extending the 1-D Hovel Model for Coherent and Incoherent Back Reflections in Homojunction Solar Cells," *IEEE Journal of Quantum Electronics*, vol. 49, no. 5, pp. 462–470, May 2013, doi: 10.1109/JQE.2013.2252148.

[42] C. C. Katsidis and D. I. Siapkas, "General transfer-matrix method for optical multilayer systems with coherent, partially coherent, and incoherent interference," *Appl. Opt.*, vol. 41, no. 19, p. 3978, Jul. 2002, doi: 10.1364/AO.41.003978.

[43] Md. S. Islam, "Analytical modeling of organic solar cells including monomolecular recombination and carrier generation calculated by optical transfer matrix method," *Organic Electronics*, vol. 41, pp. 143–156, Feb. 2017, doi: 10.1016/j.orgel.2016.10.040.

[44] D. L. Lepkowski, J. T. Boyer, D. J. Chmielewski, A. C. Silvaggio, S. A. Ringel, and T. J. Grassman, "Investigation of Rear-Emitter GaAsP Top Cells for use in III-V/Si Tandem Photovoltaics," in *2018 IEEE 7th World Conference on Photovoltaic Energy Conversion (WCPEC) (A Joint Conference of 45th IEEE PVSC, 28th PVSEC 34th EU PVSEC)*, Jun. 2018, pp. 2642–2647. doi: 10.1109/PVSC.2018.8547748.

[45] B. Wernsman, "Effect of Graded Base p-Doping on MIM Performance," in *AIP Conference Proceedings*, Rome (Italy): AIP, 2003, pp. 488–497. doi: 10.1063/1.1539404.

[46] Y. Kim *et al.*, "Efficiency Enhancement of InGaP/InGaAs/Ge Solar Cells with Gradually Doped P-N Junction Active Layers," in *2017 IEEE 44th Photovoltaic Specialist Conference (PVSC)*, Jun. 2017, pp. 244–246. doi: 10.1109/PVSC.2017.8366712.

[47] "Mike Grundmann." Accessed: May 19, 2023. [Online]. Available: http://my.ece.ucsb.edu/mgrundmann/bandeng/

[48] R. A. Sinton and A. Cuevas, "Contactless determination of current–voltage characteristics and minority-carrier lifetimes in semiconductors from quasi-steady-state photoconductance data," *Appl. Phys. Lett.*, vol. 69, no. 17, pp. 2510–2512, Oct. 1996, doi: 10.1063/1.117723.

[49] S. Hegedus, D. Desai, and C. Thompson, "Voltage dependent photocurrent collection in CdTe/CdS solar cells," *Progress in Photovoltaics: Research and Applications*, vol. 15, no. 7, pp. 587–602, 2007, doi: 10.1002/pip.767.

[50] A. M. Bothwell, J. A. Drayton, and J. R. Sites, "Performance Analysis of 0.4–1.2-µm CdTe Solar Cells," *IEEE Journal of Photovoltaics*, vol. 10, no. 1, pp. 259–266, Jan. 2020, doi: 10.1109/JPHOTOV.2019.2947556.

[51] A. L. Fahrenbruch and R. H. Bube, *Fundamentals of solar cells: photovoltaic solar energy conversion*. New York: Academic Press, 1983.

[52] M. Yamaguchi, A. Yamamoto, and Y. Itoh, "Effect of dislocations on the efficiency of thin-film GaAs solar cells on Si substrates," *Journal of Applied Physics*, vol. 59, no. 5, pp. 1751–1753, Mar. 1986, doi: 10.1063/1.336439.